International Journal of Solids and Structures 241 (2022) 111509

Contents lists available at ScienceDirect

International Journal of Solids and Structures

journal homepage: www.elsevier.com/locate/ijsolstr

Revisiting the interaction of highly nonlinear solitary wave with wall: From infinite to finite thickness

Qing Peng [a], Xiaoming Liu [a,b,*], Xinghua Shi [c], YueGuang Wei [d]

[a] LNM, Institute of Mechanics, Chinese Academy of Sciences, Beijing 100190, China
[b] School of Engineering Science, UCAS, Beijing 100049, China
[c] Laboratory of Theoretical and Computational Nanoscience, National Center for Nanoscience and Technology, Chinese Academy of Sciences, Beijing 100190, China
[d] College of Engineering, Peking University, Beijing 100871, China

ARTICLE INFO

Keywords:
Highly nonlinear solitary wave
Reflection on plate
Monodispersed granular chain
Sphere-plate contact
Non-destructive evaluation

ABSTRACT

The classical reflection of a highly nonlinear solitary wave (HNSW) on an elastic wall has been used to determine the material properties of the wall, but does not work on a plate (a wall with finite thickness). In this paper, by coupling sphere-plate contact with chain dynamics, we revealed that: with the same initial velocity, the energy dissipation of multi-sphere plate impact is different from the single sphere plate impact, but the contact force on the plate performs similarly. Based on this fact, we then developed two universal force models considering the dissipative feature of the plate. These force models (reflection force on the chain and contact force on the plate) can universally connect the signals of the HNSW with the dissipative feature of the plate. With the obtained force models, we proposed a non-destructive evaluation method, which can identify both the plate material and thickness by measuring the two forces: the reflection force on the chain and the contact force on the plate. Agreement with finite element simulations suggests that non-destructive evaluation of thin-walled structure can be realized by using HNSW with the proposed method.

1. Introduction

The Newton's Cradle experiment (Herrmann and Schmälzle, 1981; Herrmann and Seitz, 1982) revealed one type of dispersion-free waves. This type of wave, travelling on a chain of unloaded or weakly compressed monodispersed elastic spheres, was categorized as highly nonlinear solitary waves (HNSWs). The essential feature of HNSW is that the wave can propagate along the chain without energy loss, so that the wave profile can be kept unchanged during the propagation (Lazaridi and Nesterenko, 1985; Nesterenko, 1984). As a result, the high propagation quality of the HNSW signal can be applied widely in industry. For instance, studies were performed on the propagation of HNSWs through single granular chain (Chatterjee, 1999; Coste et al., 1997; Daraio et al., 2005; Hasan and Nemat-Nasser, 2017; MacKay, 1999; Sen et al., 2008; Sen and Manciu, 2001; Sinkovits and Sen, 1995; Wang et al., 2014; Waymel et al., 2018), granular network (Daraio et al., 2010; Leonard et al., 2014; Ngo et al., 2012), a chain of cylinders (Yang et al., 2020), and the stability of traveling HNSWs (Liu et al., 2021; Liu et al., 2019). These studies laid a theoretical foundation for the mechanism of wave propagation in granular matter and guided the design of granular structure with required purposes, such as phononic crystals (Chaunsali et al., 2017; Kim and Yang, 2014; Kim et al., 2019), energy trapper (Daraio et al., 2006), and acoustic lens (Spadoni and Daraio, 2010).

How an HNSW interacts with an elastic object or an interface was studied within a few decades; the obtained results can be used for inferring properties of the object or interface. For example, Job et al. studied the interaction of an HNSW against an elastic wall (Job et al., 2005), providing an analytical solution to predict the force between the granular chain and the wall. The interaction of HNSW with an interface of two granular chains was reported experimentally by Nesterenko, et al. (Nesterenko et al., 2005) and numerically by Vergara (Vergara, 2005), showing that the interaction highly depends on the high gradient of particle velocity around the interface. In another study, the interaction of HNSW with a linear elastic medium was studied by Yang et al. (Yang et al., 2011) both experimentally and theoretically, revealing that the travel time of HNSW and force magnitudes of the primary and secondary reflected waves are strongly associated with the elasticity and geometry of target. These studies have shown the potential of the HNSW being an effective non-destructive evaluation tool for identification of mechanical properties (Job et al., 2005; Villacreses et al., 2021; Yang et al., 2011), detection of defects in bulk medium (Khatri et al., 2008; Sen

* Corresponding author at: LNM, Institute of Mechanics, Chinese Academy of Sciences, Beijing 100190, China.
E-mail address: xiaomingliu@imech.ac.cn (X. Liu).

https://doi.org/10.1016/j.ijsolstr.2022.111509
Received 6 September 2021; Received in revised form 18 January 2022; Accepted 10 February 2022
Available online 14 February 2022

Nomenclature

B_i	The i-th sphere
B_p	Plate
E_s	Young's modulus of sphere
E_p	Young's modulus of plate
E_{ss}	Effective modules of sphere-sphere contact
E_{sp}	Effective modules of sphere-plate contact
E^{flx}	Energy dissipation by flexural wave
$\overline{E^{flx}}$	Non-dimensional energy dissipation by flexural wave
$\overline{E^{kin}}$	Total non-dimensional kinetic energy
$E^{pot}_{i,i+1}$	Potential energy between the i-th and the $(i+1)$-th spheres
E^{pot}_p	Potential energy between the N-th sphere and plate
$\overline{E^{pot}_{i,i+1}}$	Non-dimensional potential energy between the i-th and the $(i+1)$-th spheres
$\overline{E^{pot}_p}$	Non-dimensional potential energy between the N-th sphere and plate
F	Force
$\overline{F}$	Non-dimensional force
$F_{i,i+1}$	Contact force between the i-th and the $(i+1)$-th spheres
F_p	Contact force between the end sphere and the plate
F_8	Force detected by the sensor embedded in the center of the eighth sphere
H	Thickness of plate
k_{ss}	Contact stiffness between spheres
k_{sp}	Contact stiffness between sphere and plate
m	Mass of sphere
N	Number of spheres
R	Radius of sphere
r_i	Correlation coefficients between Π_i and $\overline{E^{flx}}$
s_i	Non-dimensional position of the i-th sphere
s_p	Non-dimensional position of plate
t	Time
T	Coefficient for time normalization
V_0	Initial impact velocity
x_i	Position of the i-th sphere
x_p	Position of plate
y_i	State variables,$i = 1, \cdots, 2N+2$
α	Material dependent coefficient
β	Fraction of potential energy before the solitary wave impacting on plate
$\delta_{i,i+1}$	Compressive displacement between the i-th sphere and the $(i+1)$-th sphere
δ_p	Compressive displacement between the end sphere and plate
$\overline{\delta}_p$	Non-dimensional compressive displacement between the end sphere and plate
η_A	Amplitude ratio of reflected wave (ARR)
η_F	Ratio of contact force on plate to contact force on chain
ν_s	Poisson's ratio of sphere
ν_p	Poisson's ratio of plate
ρ_s	Density of sphere
ρ_p	Density of plate
λ	Zener's inelastic parameter of plate
τ	Non-dimensional time

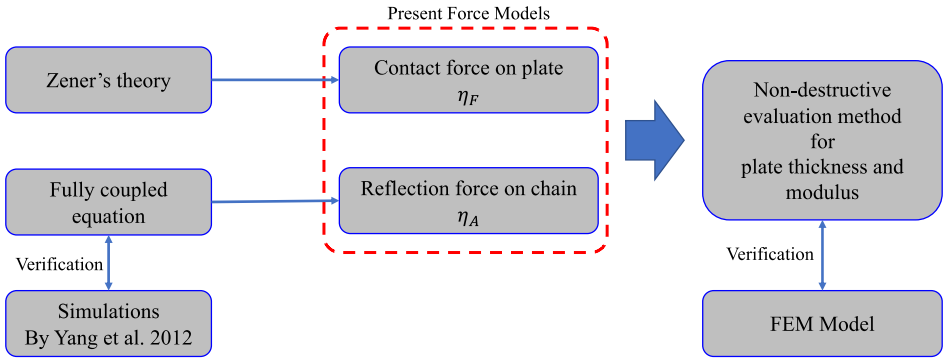

Fig. 1. Roadmap of present study.

et al., 2005, 1998; Yang et al., 2013), and reconstruction of microstructures of the tested target (Yoon et al., 2020). In these applications, the tested targets were assumed to be infinitely thick. In a real situation, however, the tested targets have a finite thickness, so the flexural wave induced by the structure compliance will dissipate a large fraction of the energy. Therefore, it is possible to utilize the reflection feature of HNSW for detecting on thin-walled structures accurately/properly only when the exact amount of the dissipated energy is known.

The key question remained is: how is the difference of the interaction of an HNSW with a thin plate from the interaction model with a wall? To the best of our knowledge, there is no universal interaction law for the reflection of an HNSW against a thin plate, except a few cases which attempt to apply the HNSW to detect on the thin-walled structures, such as composite beams (Schiffer and Kim, 2019), plate corrosions (Jalali and Rizzo, 2021, 2020), implant composites (Berhanu et al., 2012), textiles (Nasrollahi et al., 2019), and the human cornea (Nasrollahi and Rizzo, 2020). When the structure is thin, energy dissipation by flexural waves cannot be ignored (Yang et al., 2012); this fact renders the previous model (Job et al., 2005) invalid for the thin-walled structures. Although recent studies have highlighted the effects of compliance on the reflected wave (Cai et al., 2014, 2014, 2013; Nasrollahi et al., 2019; Nasrollahi and Rizzo, 2020; Zhang et al., 2020), these effects tended to be on a case-specific basis, thus requiring separate finite element simulations. These simulations were not able to provide one universal law describing the non-conservative interaction of an HNSW with a thin plate.

In this paper, by coupling the sphere-plate contact (Zener, 1941) with chain dynamics, we developed two force models of HNSW reflection from a plate of finite thickness as shown in Fig. 1. With these force models, we proposed a non-destructive identification method to predict the modulus and thickness of plate by measuring the amplitude ratio of reflected wave (ARR) in the chain and the contact force on the plate.

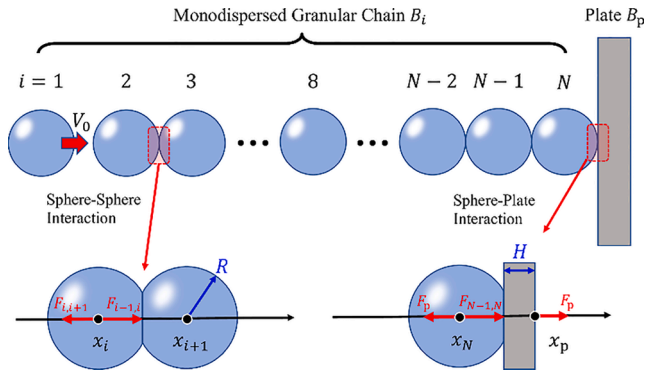

Fig. 2. Schematic diagram for interaction of monodispersed granular chain and plate. The contact forces between each neighboring pair obeys Hertz's contact relationship.

This paper is organized as follows. In Section 2, we built up the non-dimensional control equations for the system by coupling the Hertz-type contact for the chain and Zener-type contact for the plate. In Section 3, we studied the dependencies of the non-dimensional parameters on the energy dissipation by flexural wave. In Section 4, we developed two universal force models considering the dissipative feature of the plate. In Section 5, based on the obtained force models, we proposed a non-destructive evaluation method for the identification of plate material property and thickness. Finally, in Section 6, we summarized conclusions and remarked on the proposed models about their advantages and limitations.

2. Coupled equation for a solitary wave against a plate

Fig. 2 illustrates a monodispersed granular chain of N spheres impacting a large plate. A compactly supported HNSW is generated on the granular chain by the impact of the leading sphere with velocity V_0. During the HNSW propagation, each sphere interacts with its neighbors, obeying the Hertz contact relationship (Heinrich Hertz, 1882). When the HNSW impact on the plate, the end sphere interacts with the plate, obeying Zener's sphere-plate contact relationship (Zener, 1941). After the interaction, the HNSW reflects backward. In this section, we formulate the dynamics by coupling the Hertz-type interaction between spheres and the Zener-type interaction between sphere and plate as follows.

2.1. Interaction of the chain and plate

During the first stage, the HNSW travels forward such that kinetic energy is converted into potential energy and vice versa. The potential energy between the i-th sphere and the $(i+1)$-th sphere in contact corresponds to the Hertzian potential, $E^{\text{pot}}_{i,i+1} = \frac{2}{5}k_{\text{ss}}\delta^{\frac{5}{2}}_{i,i+1}$, where $\delta_{i,i+1} = 2R + x_i - x_{i+1}$ is the compressive displacement between the spheres, x_i is the position of the i-th sphere, k_{ss} is the contact stiffness between spheres given by $k_{\text{ss}} = \frac{4}{3}\sqrt{\frac{R}{2}}E_{\text{ss}}$, R is the radius of sphere, $E^{-1}_{\text{ss}} = \frac{2\left(1-\nu^2_{\text{s}}\right)}{E_{\text{s}}}$, and E_{s} and ν_{s} are the Young's modulus and Poisson's ratio of the sphere, respectively. The total potential energy of the chain can be obtained by summing all contact pairs, $E^{\text{pot}}_{\text{chain}} = \sum_{i=1}^{N-1}E^{\text{pot}}_{i,i+1}$, and the total kinetic energy is $E^{\text{kin}}_{\text{chain}} = \frac{1}{2}m\sum_{i=1}^{N}\dot{x}^2_i$, where m is the mass of sphere.

During the interaction stage, as a fraction of the energy is converted into the contact potential between the sphere and plate, another fraction is dissipated simultaneously by the flexural wave on the plate. The potential energy between the end sphere and plate is $E^{\text{pot}}_{\text{p}} = \frac{2}{5}k_{\text{sp}}\delta^{\frac{5}{2}}_{\text{p}}$, where $\delta_{\text{sp}} = R + H + x_N - x_{\text{p}}$ is the compressive displacement between the end sphere and the plate, x_{p} is the position of the plate, H is the thickness of the plate, $k_{\text{sp}} = \frac{4}{3}\sqrt{RE}_{\text{sp}}$, $E^{-1}_{\text{sp}} = \frac{1-\nu^2_{\text{s}}}{E_{\text{s}}} + \frac{1-\nu^2_{\text{p}}}{E_{\text{p}}}$, and E_{p} and ν_{p} are the Young's modulus and Poisson's ratio of the plate, respectively. The dissipated energy on the plate has the form: $E^{\text{flx}} = \int F_{\text{p}}\text{d}x_{\text{p}}$, where F_{p} is the contact force between the end sphere and the plate.

To couple the chain dynamics with the plate dynamics, we need to find the relationship between the contact force F_{p} and the position of the plate x_{p}. Zener used the method of modal decomposition to obtain the relationship between the contact force and the displacement of plate (Zener, 1941), briefly as follows.

By modal decomposition, Zener assumed the displacement field on plate could be expressed as:

$$U(x,y,t) = \sum_n C_n(t)U_n(x,y) \tag{1}$$

Substituting Eq. (1) to the wave equation of plate, he obtained

$$\left(\frac{\text{d}^2}{\text{d}t^2} + \omega^2_k\right)C_k = \frac{1}{\rho_{\text{p}}H}\int U_k Z dS \tag{2}$$

where ρ_{p} is the density of the plate and Z is the surface density of the normal force. Treating the contact force as a point force, Eq. (2) becomes

$$\left(\frac{\text{d}^2}{\text{d}t^2} + \omega^2_k\right)C_k = \frac{1}{\rho_{\text{p}}H}U_k(0)F_{\text{p}} \tag{3}$$

Then, solving C_k and substituting it into Eq. (1), Zener got

$$\begin{aligned} x_{\text{p}} &= \frac{1}{\rho_{\text{p}}H}\sum_n \omega^{-1}_n U^2_n(0) \times \int_0^t F_{\text{p}}(t')\sin\omega_n(t-t')\text{d}t' \\ &= \frac{1}{\rho_{\text{p}}H}\int_0^t F_{\text{p}}(t')\left(\sum_n \omega^{-1}_n U^2_n(0)\sin\omega_n(t-t')\right)\text{d}t' \end{aligned} \tag{4}$$

Averaging $U^2_n(0)$ in modal space admits the following identity:

$$\sum_n \omega^{-1}_n U^2_n(0)\sin\omega_n(t-t') = \frac{1}{8}\left(\frac{\rho_{\text{p}}H}{D}\right)^{\frac{1}{2}}$$

where $D = \frac{1}{12}H^3\frac{E_{\text{p}}}{1-\nu^2_{\text{p}}}$. Hence, Eq. (4) becomes

$$x_{\text{p}} = \alpha\int_0^t F_{\text{p}}(t')\text{d}t' \tag{5}$$

or equivalently

$$\dot{x}_{\text{p}} = \alpha F_{\text{p}} \tag{6}$$

where

$$\alpha = \frac{1}{4\rho_{\text{p}}H^2}\sqrt{\frac{3\rho_{\text{p}}\left(1-\nu^2_{\text{p}}\right)}{E_{\text{p}}}} \tag{7}$$

is a parameter that depends on the material properties and the plate thickness. Eq. (5) and Eq. (6) indicate that for a large plate, the time-derivate of the plate deflection is proportional to the contact force on the plate. In the following section, the sphere-plate interaction as described in Eq. (6) will be used for the fully coupled formulation.

It should be noted that Zener implied the following assumptions:

1) Point-force assumption: the size of contact area is small in comparison with the plate thickness, so that the contact force can be viewed as a concentrated force.
2) Large-plate assumption: the flexural wave on plate should not return from the boundary during the interaction of the ending sphere and the plate.

As for the point-force assumption, we can adapt the chain design and limit the impact speed. As long as the contact radius is smaller than the

thickness of the plate, we can treat the distributed force as a point force and the present model stays valid. As for the large-plate assumption, the boundary condition is critical for developing the present models. This boundary effect has been studied by Yang et al. (Yang et al., 2012), who conclude that the boundary will have little effect if the impact position is away from the boundary with a distance larger than a critical distance L_c. Also, they suggested that the critical distance L_c is less than ten times the sphere size in most of the cases. In practice, the sphere size is much smaller than the plate, so that the critical distance will be much smaller than the size of tested plate. In another words, if we locate the impact position away from the boundary with a distance of ten times sphere size, which is very small compared with the size of tested plate, we can treat the plate as infinitely large so that Zener's contact for sphere-plate can be applied.

2.2. Dimensional analysis on the coupled equations

Coupling the Hertz-type interaction for the spheres and Zener-type interaction for the sphere and the plate, we obtain the complete equations for the system, as follows:

$$\begin{cases} m\ddot{x}_{i<N} &= k_{ss}\left(\delta_{i-1,i}^{\frac{3}{2}} - \delta_{i,i+1}^{\frac{3}{2}}\right) \\ m\ddot{x}_N &= k_{ss}\delta_{N-1,N}^{\frac{3}{2}} - k_{sp}\delta_p^{\frac{3}{2}} \\ \ddot{x}_p &= \alpha\dfrac{\mathrm{d}F_p}{\mathrm{d}t} \end{cases} \tag{8}$$

with an initial condition $\dot{x}_1\Big|_{t=0} = V_0$, where V_0 is the impact velocity. By variable substitution:

$$\begin{cases} T &= m^{\frac{2}{5}}k_{ss}^{-\frac{2}{5}}V_0^{-\frac{1}{5}} \\ \tau &= \dfrac{t}{T} \\ s_i &= \dfrac{x_i}{TV_0} \end{cases} \tag{9}$$

we can normalize Eq. (8) to be non-dimensional and hence mathematically universal, as follows:

$$\begin{cases} \ddot{s}_{i<N} &= (2\Pi_1 + s_{i-1} - s_i)^{\frac{3}{2}} - (2\Pi_1 + s_i - s_{i+1})^{\frac{3}{2}} \\ \ddot{s}_N &= (2\Pi_1 + s_{N-1} - s_N)^{\frac{3}{2}} - \Pi_3\left(\Pi_1 + \dfrac{\Pi_1}{\Pi_2} + s_N - s_p\right)^{\frac{3}{2}} \\ \ddot{s}_p &= \dfrac{3}{2}\Pi_4\Pi_3^{\frac{3}{2}}\left(\Pi_1 + \dfrac{\Pi_1}{\Pi_2} + s_N - s_p\right)^{\frac{1}{2}}(\dot{s}_N - \dot{s}_p) \end{cases} \tag{10}$$

with initial condition $\dot{s}_1\Big|_{\tau=0} = 1$, where

$$\begin{cases} \Pi_1 = \dfrac{R}{TV_0} \\ \Pi_2 = \dfrac{R}{H} \\ \Pi_3 = \dfrac{k_{sp}}{k_{ss}} \\ \Pi_4 = \lambda \end{cases} \tag{11}$$

and λ is the inelastic parameter defined by Zener (Zener, 1941):

$$\lambda = \frac{\pi^{\frac{3}{5}}}{3^{\frac{1}{2}}}\left(\frac{R}{H}\right)^2\left(\frac{V_0}{V_W}\right)^{\frac{1}{5}}\left(\frac{\rho_s}{\rho_p}\right)^{\frac{3}{5}}\left(\frac{E_s/\left(1-\nu_s^2\right)}{E_s/\left(1-\nu_s^2\right) + E_p/\left(1-\nu_p^2\right)}\right)^{\frac{2}{5}} \tag{12}$$

where $V_W = \sqrt{E_p/\rho_p\left(1-\nu_p^2\right)}$ is the propagation velocity of quasi-longitudinal waves in thin plates. We can see that the entire system is controlled by only four non-dimensional parameters: $\Pi_1 = RV_0^{-\frac{4}{5}}k_{ss}^{\frac{2}{5}}m^{-\frac{2}{5}}$ is related to the initial velocity, Π_2 represent the geometrical information, Π_3 stands for the contact properties, and Π_4 serves as the dissipation of the plate.

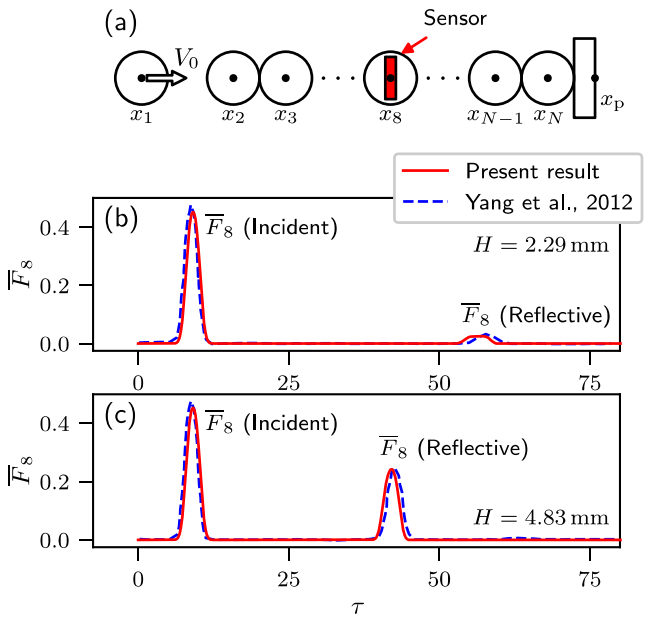

Fig. 3. Comparison of the present results with the simulations by Yang et al., 2012: (a) numerical set-up, (b) plate thickness $H = 2.29$mm, and (c) plate thickness $H = 4.83$mm.

To solve Eq. (10), we convert governing equations into a dynamical system. By introducing the following state variable:

$$\begin{cases} y_i &= s_i, \quad for\ i = 1, 2, \cdots, N \\ y_{N+1} &= s_p \\ y_{N+1+i} &= \dot{s}_i, \quad for\ i = 1, 2, \cdots, N \\ y_{2N+2} &= \dot{s}_p \end{cases} \tag{13}$$

we thus obtain a dynamical system:

$$\begin{cases} \dot{y}_i &= y_{N+1+i}, \quad for\ i = 1, 2, \cdots, N+1 \\ \dot{y}_{N+2} &= -(2\Pi_1 + y_1 - y_2)^{\frac{3}{2}} \\ \dot{y}_{N+1+i} &= (2\Pi_1 + y_{i-1} - y_i)^{\frac{3}{2}} - (2\Pi_1 + y_i - y_{i+1})^{\frac{3}{2}}, \quad for\ i = 2, \cdots, N-1 \\ \dot{y}_{N+1+i} &= (2\Pi_1 + y_{N-1} - y_N)^{\frac{3}{2}} - \Pi_3\left(\Pi_1 + \dfrac{\Pi_1}{\Pi_2} + y_N - y_{N+1}\right)^{\frac{3}{2}} \\ y_{2N+2} &= \dfrac{3}{2}\Pi_4\Pi_3^{\frac{3}{2}}\left(\Pi_1 + \dfrac{\Pi_1}{\Pi_2} + y_N - y_{N+1}\right)^{\frac{1}{2}}(y_{2N+1} - y_{2N+2}) \end{cases} \tag{14}$$

with the initial state at $\tau = 0$:

$$\begin{cases} y_i &= 2(i-1)\Pi_1, for 1 \le i \le N \\ y_{N+1} &= 2(N-1)\Pi_1 + \dfrac{\Pi_1}{\Pi_2} \\ y_{N+2} &= 1 \\ y_i &= 0, for\ i \ge N+3 \end{cases} \tag{15}$$

and the dynamical system Eq. (14) and (15) can be solved with Runge-Kutta method.

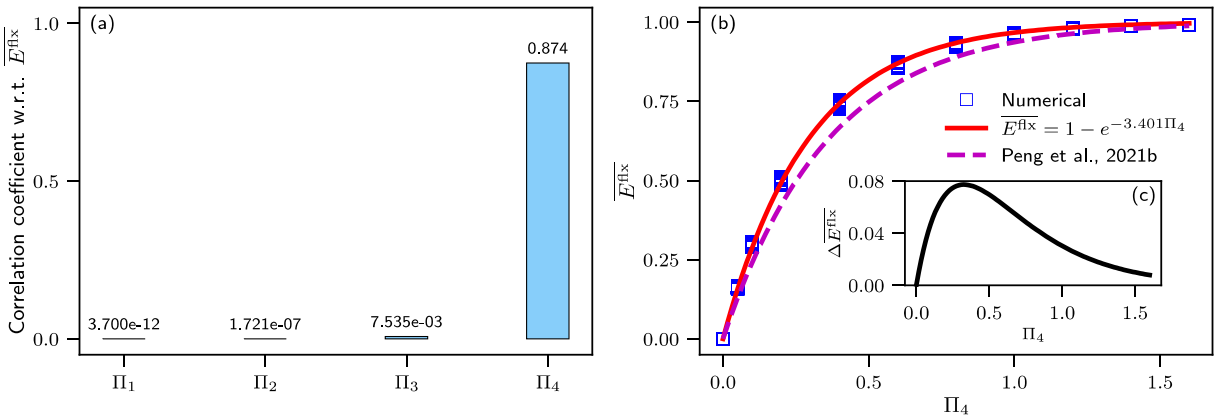

Fig. 4. (a) Correlation coefficient of non-dimensional parameters with respect to energy dissipation by flexural wave. (b) Non-dimensional energy dissipation by flexural wave as a function of Π_4. Square markers represent more than 20,000 numerical results. Inset (c) shows difference between present model and previous model (Peng et al., 2021b).

2.3. Verification of the numerical solutions to the coupled equations

By using the Runge-Kutta method, we numerically solved Eq. (14) and (15) and verified the results with Yang's simulation (Yang et al., 2012). In their simulations, the set-up comprised a granular chain of 20 spheres and a plate. The diameter of sphere was 9.53 mm and the thickness of plate was set to 2.29 mm and 4.83 mm individually to study the effect of plate thickness. The material of spheres was stainless steel, with elastic modulus 200 GPa, Poisson's ratio 0.28, and density 7800 kg/m^3. The material of plate was aluminum, with elastic modulus 68.9 GPa, Poisson's ratio 0.33, and density 2360 kg/m^3. The initial impact velocity was set to 0.31 m/s to produce the HNSW. For the case of the plate thickness being 2.29 mm, Π_1, Π_2, Π_3, and Π_4 are 1012.0, 2.08, 0.743, and 1.26, respectively; for the case of the plate thickness being 4.83 mm, Π_1, Π_2, Π_3, and Π_4 are 1012.0, 0.987, 0.743, and 0.284, respectively. To model the impact, Yang et al. coupled a discrete element model with a spectral element model to simulate both the HNSW on the chain and the wave propagation in the thin plate (Yang et al., 2012). Unlike their case-by-case model, we adopted a fully coupled dynamical system and thus made a non-dimensional universal formulation possible. Fig. 3 shows a comparison of the results between the present coupled dynamical model and the simulation results of Yang et al., where agreements can be found for both cases. In Fig. 3, we use a non-dimensional force defined as the following expression:

$$\overline{F} = \frac{F}{k_{ss}^{\frac{2}{5}} m^{\frac{3}{5}} V_0^{\frac{6}{5}}} \tag{16}$$

It should be noted that the simulation results of Yang et al. were validated by their experiments. In the experiment, they measured the force with a sensor embedded in the middle of the eighth sphere (Yang et al., 2012) as shown in Fig. 3(a); thus, by equilibrium, the detected force signal ($\overline{F}_8$) is the average of the forces between the 7th and the 8th spheres and between the 8th and the 9th spheres: $\overline{F}_8 = \frac{1}{2}\left(\overline{F}_{7,8} + \overline{F}_{8,9}\right)$.

3. Energy dissipation by flexural wave

To study the problem systematically, we extended the values of the four non-dimensional parameters to accommodate most scenarios. Π_1 varied from 10.0 to 2000.0, to cover a wide range of impact speeds. For example, in Yang's study, an initial velocity of 0.31 m/s was used, corresponding to a Π_1 value of about 1012.0 (Yang et al., 2012). Π_2 varied from 0.01 to 100.0, such that the plate thickness ranged from $0.01R$ to $100R$, covering most practical scenarios. For example, using the chain (R = 13 mm) as Job et al. did (Job et al., 2005), we can accommodate cases with the plate thicknesses ranging from 0.13 mm to 1300 mm. Π_3 varied from 0.05 to 2.0, such that the plate could be very soft or very hard. Π_4 varied from 0 to 1.6, so that the system transited from one that was non-dissipative to one that was highly dissipative; notably, the inelastic coefficient $\lambda = \Pi_4 = 1.6$ leads to a very low coefficient of restitution (about 0.053, corresponding to a high energy dissipation: 99.7%) (Mueller et al., 2015; Zener, 1941).

To find that how Π_1, Π_2, Π_3, and Π_4 affects the energy dissipation by flexural wave $\overline{E^{\text{flx}}}$, we calculated the correlation coefficients of Π_1, Π_2, Π_3, and Π_4 with respect to the energy dissipation $\overline{E^{\text{flx}}}$ as follows:

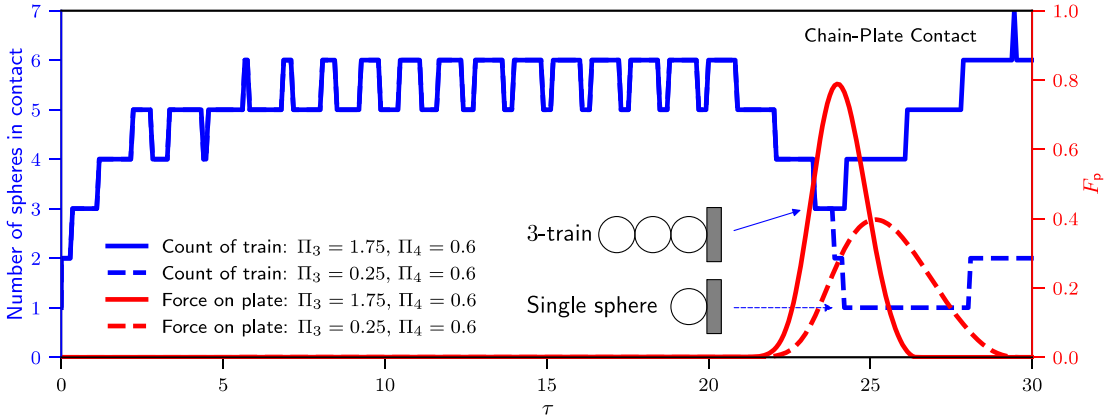

Fig. 5. Examples of histories of number of spheres in contact and non-dimensional contact force on plate during interaction of solitary wave with plate in case of Π_1 and Π_2 being 10.0 and 2.5, respectively.

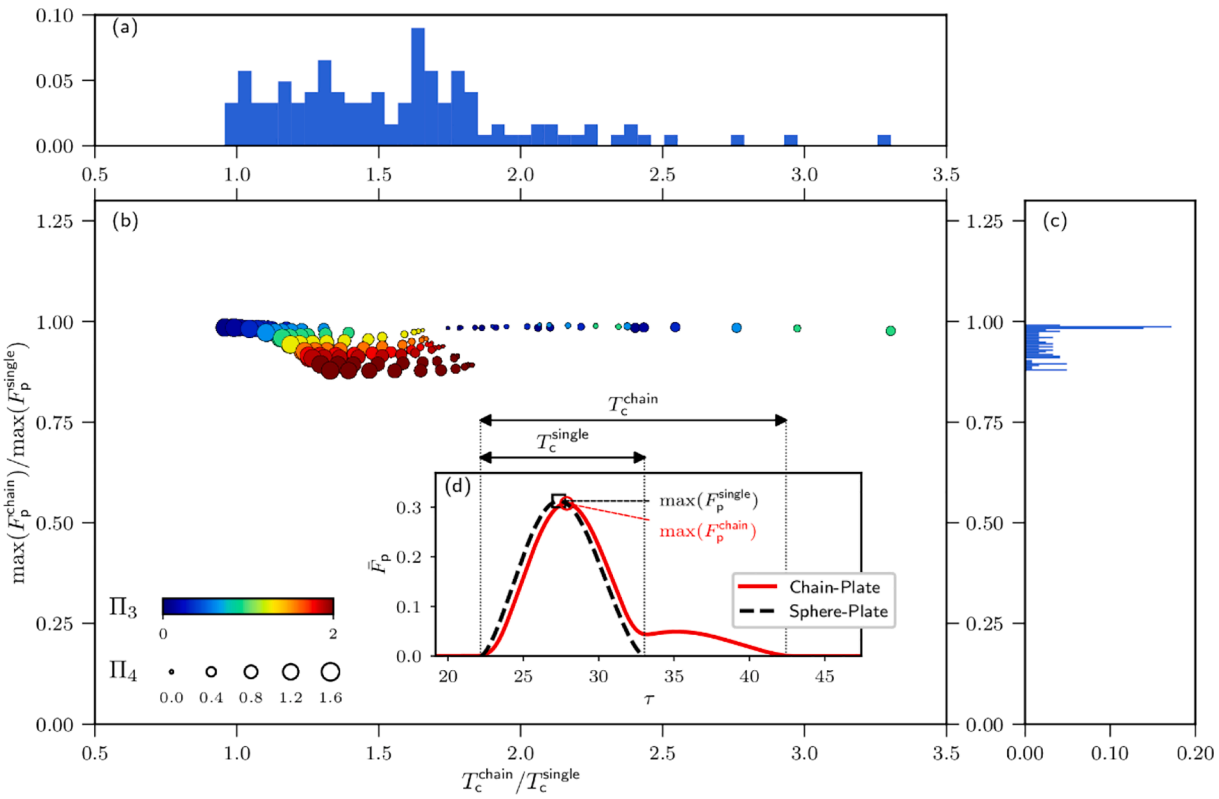

Fig. 6. Scatter plot with marginal histograms for maximal contact forces on plate and contact times of present numerical results: (a) normalized distribution of contact times, (b) main scatter plot, and (c) normalized distribution of maximal contact forces. Inset (d) shows typical contact time histories of chain-plate interaction and sphere-plate interaction.

$$r_i\left(\Pi_i, \overline{E^{\text{f1x}}}\right) = \frac{\text{Cov}\left(\Pi_i, \overline{E^{\text{f1x}}}\right)}{\sqrt{\text{Var}(\Pi_i)\text{Var}\left(\overline{E^{\text{f1x}}}\right)}}, i = 1, 2, 3, 4 \tag{17}$$

where $\text{Cov}\left(\Pi_i, \overline{E^{\text{f1x}}}\right)$ is the covariance of Π_i and $\overline{E^{\text{f1x}}}$, and $\text{Var}(\Pi_i)$ and $\text{Var}\left(\overline{E^{\text{f1x}}}\right)$ are the variances of Π_i and $\overline{E^{\text{f1x}}}$, respectively.

As shown in Fig. 4(a), with more than 20,000 simulations, the correlation coefficients of Π_1, Π_2, and Π_3 with respect to the energy dissipation is significantly smaller those of Π_4, showing that $\overline{E^{\text{f1x}}}$ can be approximated by a single variable function of Π_4. The correlation coefficient of Π_4 also indicates that $\overline{E^{\text{f1x}}}$ increases with an increasing Π_4 in a statistical manner. In fact, as $\Pi_4 = \lambda$ represents the inelasticity of the end sphere impacting the plate (Zener, 1941), we show in Fig. 4(b) that as Π_4 increases, more energy is dissipated by flexural wave. After inspecting all the numerical results (more than 20,000) of Eq. (10), we obtain an explicit expression for the energy dissipation as shown in Fig. 4:

$$\begin{cases} \overline{E^{\text{f1x}}} & = 1 - e^{-\alpha\Pi_4} \\ \alpha & = 3.401 \end{cases} \tag{18}$$

or equivalently:

$$E^{\text{f1x}} = \frac{1}{2} m V_0^2 (1 - e^{-\alpha\Pi_4}) \tag{19}$$

where α is a coefficient characterize the energy dissipation with respect to Π_4.

Notably, the energy dissipation of a chain impacting on a plate is different from that of a single sphere impacting on a plate. In our previous study (Peng et al., 2021b), for one sphere impacting on a large plate, we obtained the coefficient for energy dissipation as follows:

$$\alpha_p = 2.755 \tag{20}$$

which is smaller than the present one, $\alpha = 3.401$. This suggests that the energy dissipation of a chain versus a plate is greater than that of one sphere versus a plate as shown by Fig. 4(b), and the difference is shown in Fig. 4(c). The reason for such phenomenon is that a train of multiple spheres (k-train) participates in the impacting process. As shown in Fig. 5, we could find a 5-train or 6-train before the chain-plate interaction; in another word, a solitary wave supported by 5 or 6 consecutive spheres travels towards the plate. For the interaction with a harder plate (higher contact stiffness), the 5-train is shortened to a 3-train that is kept for most of the interaction period. While for the interaction with a softer plate (lower contact stiffness), the 5-train becomes single sphere for most of the interaction period. Different from single sphere impacting on a plate, a train of spheres implies higher inertia with the same energy and momentum, and thus results in longer impacting time.

In our previous study, we proposed an analytical solution to the Zener problem of single sphere impacting plate (Peng et al., 2021b). As a result, the impact time T_c^{single} and the maximal impact force $\max(F_p^{single})$ for the single sphere case can be derived analytically. With the present simulation to Eq. (10), we normalize the impact time of chain-plate interaction T_c^{chain} and the maximal impact force $\max(F_p^{chain})$ by T_c^{single} and $\max(F_p^{single})$, respectively. As shown in Fig. 6, we plot all 20,000 present numerical results to Eq. (10). Statistical distribution shows that the impact time of a chain on a plate T_c^{chain} is generally about $1.5T_c^{single}$ as shown in Fig. 6(a), while the normalized maximal force $\max(F_p^{chain})$ is still about $1.0\max(F_p^{single})$ as shown in Fig. 6(c). Fig. 6(d) shows a typical comparison, almost identical contact force and distinguishable longer acting time suggest more momentum is transferred from the chain to the plate and thus higher energy is dissipated by flexural wave.

In summary, we show that the energy dissipation of an HNSW on a chain with a plate obeys Eq. (18) universally. Different from the case of single sphere impacting on a plate, in the case of chain-plate impact, a

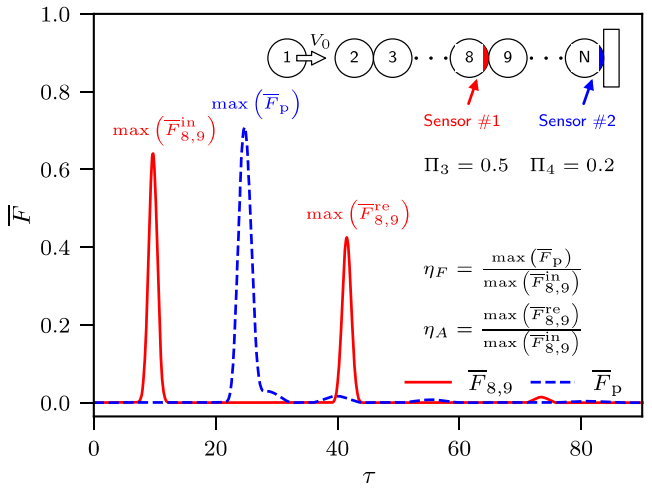

Fig. 7. Force histories of incident and reflected solitary waves and contact force histories on plate. Inset shows the set-up for the detection of force signals.

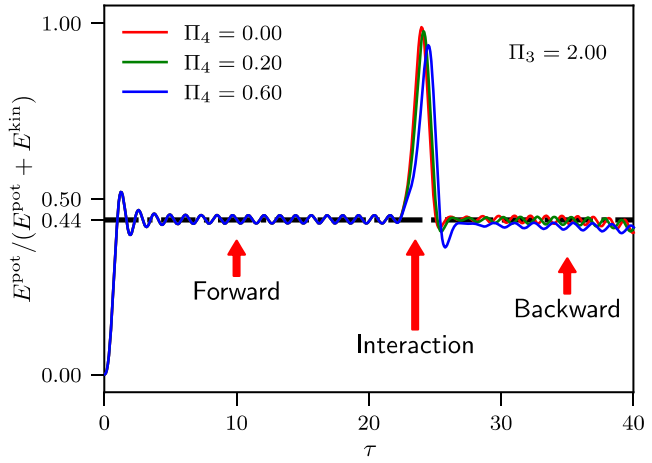

Fig. 8. History of fraction of potential energy carried by HNSW under conditions of various Π_4.

higher fraction of energy can be dissipated because of the longer impacting time by a train of multiple spheres.

4. Two proposed force models

4.1. Reflection force model in the chain

Given that only Π_4 affects energy dissipation in Section 3, we can hence obtain an expression for the amplitude ratio of reflected wave depending only on Π_4 using the signal captured by the sensor #1, as shown in Fig. 7. We define such amplitude ratio as follows:

$$\eta_A = \frac{\max\left(\overline{F}^{\mathrm{re}}_{8,9}\right)}{\max\left(\overline{F}^{\mathrm{in}}_{8,9}\right)} \tag{21}$$

where $\max\left(\overline{F}^{\mathrm{in}}_{8,9}\right)$ and $\max\left(\overline{F}^{\mathrm{re}}_{8,9}\right)$ are the maximal signals of the incident force and reflected force, respectively, detected by sensor #1.

By energy conservation, we derive the expression for η_A. Before and after the interaction of the HNSW with the plate, we have

$$E^{\mathrm{tot}}_{\mathrm{in}} = E^{\mathrm{tot}}_{\mathrm{re}} + E^{\mathrm{flx}} \tag{22}$$

where $E^{\mathrm{tot}}_{\mathrm{in}} = \frac{1}{2}mV_0^2$ and $E^{\mathrm{tot}}_{\mathrm{re}}$ are the total energy carried by the incident and reflected HNSWs. Substituting Eq. (19) into Eq. (22), we have

$$E^{\mathrm{tot}}_{\mathrm{re}} = E^{\mathrm{tot}}_{\mathrm{in}} e^{-\alpha\Pi_4} \tag{23}$$

As shown in Fig. 8, we find that the fraction of the potential energy over the total energy on the chain is about $\beta = 0.44$ for both the incident and the reflected wave; this ratio agrees with the result by Job et al. (Job et al., 2005). So, we have

$$\begin{cases} E^{\mathrm{tot}}_{\mathrm{in}} = \dfrac{1}{\beta}E^{\mathrm{pot}}_{\mathrm{in}} \\ E^{\mathrm{tot}}_{\mathrm{re}} = \dfrac{1}{\beta}E^{\mathrm{pot}}_{\mathrm{re}} \end{cases} \tag{24}$$

where $E^{\mathrm{pot}}_{\mathrm{in}}$ and $E^{\mathrm{pot}}_{\mathrm{re}}$ are the potential energy carried by the incident and reflected HNSWs. Substituting Eq. (24) into Eq. (23), we obtain:

$$E^{\mathrm{pot}}_{\mathrm{re}} = E^{\mathrm{pot}}_{\mathrm{in}} e^{-\alpha\Pi_4} \tag{25}$$

Moreover, the Hertz contact admits the following identities:

$$\begin{cases} \max\left(\overline{F}^{\mathrm{in}}_{8,9}\right) = k_{\mathrm{ss}}^{\frac{2}{5}}\left(\dfrac{5}{2}E^{\mathrm{pot}}_{\mathrm{in}}\right)^{\frac{3}{5}} \\ \max\left(\overline{F}^{\mathrm{re}}_{8,9}\right) = k_{\mathrm{ss}}^{\frac{2}{5}}\left(\dfrac{5}{2}E^{\mathrm{pot}}_{\mathrm{re}}\right)^{\frac{3}{5}} \end{cases} \tag{26}$$

Substituting Eq. (25) and (26) into Eq. (21), we have the expression for η_A:

$$\eta_A = \frac{\max\left(\overline{F}^{\mathrm{re}}_{8,9}\right)}{\max\left(\overline{F}^{\mathrm{in}}_{8,9}\right)} = \left(\frac{E^{\mathrm{pot}}_{\mathrm{re}}}{E^{\mathrm{pot}}_{\mathrm{in}}}\right)^{\frac{3}{5}} = e^{-\frac{3}{5}\alpha\Pi_4} \tag{27}$$

where $\alpha = 3.401$.

We validate Eq. (27) with the present numerical solutions to Eq. (10) as shown in Fig. 9; well agreement can be found with all 20,000 numerical results (square markers).

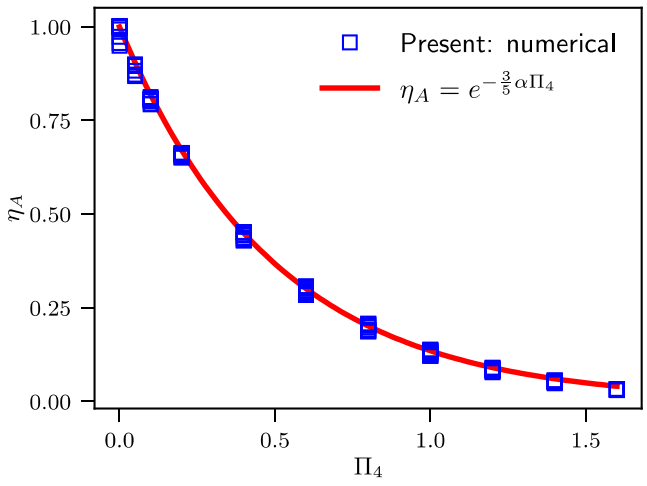

Fig. 9. Comparison of present reflection force model with present numerical solutions. Square markers represent all 20,000 numerical results.

4.2. Contact force model on the plate

The purpose of this section is to show how the contact force on the plate is affected by the plate properties: thickness and stiffness. The main difference between the reflections of HNSW against a plate and a wall is that the energy carried by the HNSW can be dissipated by the flexural wave on the plate. Unlike the reflection of the HNSW against a wall (Job et al., 2005), we show that energy dissipation by flexural wave cannot be

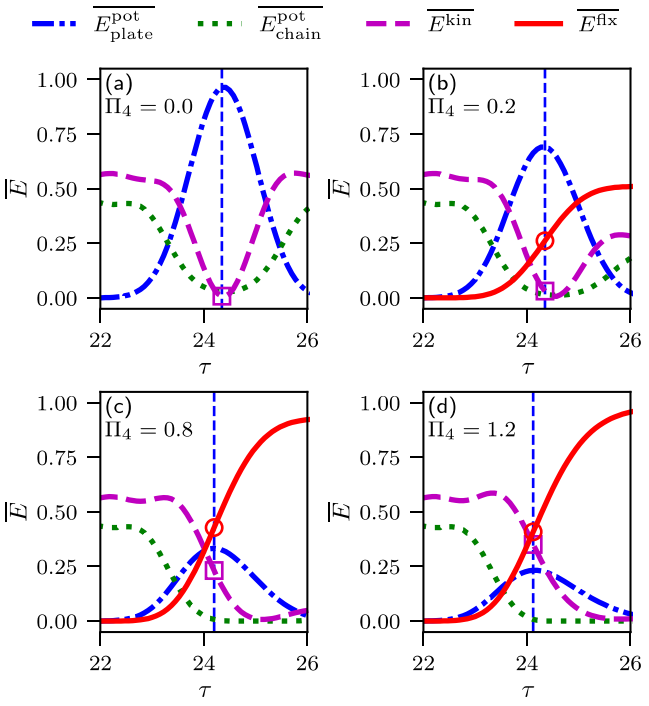

Fig. 10. Evolution of non-dimensional energy, $\overline{E} = E/(\frac{1}{2}mV_0^2)$, during the interaction between the HNSW and plate under in the cases of (a) $\Pi_4 = 0$, a wall, (b) $\Pi_4 = 0.2$, (c) $\Pi_4 = 0.8$, and (d) $\Pi_4 = 1.2$. For $\Pi_4 = 0$, the system is non-dissipative, so we omit the line for the energy dissipation by the flexural wave. In all subfigures, the middle vertical broken line marks the time when the potential energy on the plate reaches a maximum. Also, the kinetic energy and flexural dissipation are marked as a square and circle, respectively.

ignored for most cases. Here, we develop a new force model for the reflection of HNSW against a plate, making the former model (Job et al., 2005) a special case of the present force model.

4.2.1. *Why the approach of energy partition fails*

With all numerical solutions to Eq. (10), we check the energy variations during the propagation of HNSW on the chain and the interaction with the plate, and find that such energy variation in the case with a plate is very distinct from the case with a wall.

Before the HNSW hits the plate ($\tau \approx 22$), as shown in Fig. 10, the potential energy is about 44% of the total energy and the kinetic energy is about 56%, agreeing with the results of Job et al. (Job et al., 2005). In their study, this idea of energy partition is used to obtain contact force between the end sphere and tested medium. For a wall ($\Pi_4 = 0$), it can be found that the all energy that the HNSW carried is converted into potential energy between the end sphere and wall (Job et al., 2005), as shown in Fig. 10(a): both the kinetic energy and the potential energy on the chain decrease to near zero when the potential energy on the wall reaches the maximum. By energy conservation, a force model was developed (Job et al., 2005), assuming the ratio of the maximal potential energy on the plate to that on the chain is about 2, which was approximated by: $\max\left(\overline{E^{\text{pot}}_{\text{plate}}}\right)\Big/\max\left(\overline{E^{\text{pot}}_{\text{chain}}}\right) = 1/0.44 \approx 2$.

However, for a plate ($\Pi_4 > 0$), this approach of derivation cannot be applied because the relationship for the energy ratio cannot hold up when the dissipation by the flexural wave emerges. The effects of such dissipation are following:

- First, as Π_4 increases, the dissipation becomes more significant, such that the energy ratio is less than 2 at the maximal compression of contact, as shown in Fig. 10(b)-(d).
- Second, the compliance of the plate results in incomplete conversion of the kinetic energy of the chain into the potential energy between the end sphere and plate; unlike the case with a wall ($\Pi_4 = 0$), the kinetic energy of the chain is greater than zero at the maximal compression in the cases with large Π_4, as shown in Fig. 10(c) and Fig. 10(d).

As a result, to find a correct contact force model considering the energy dissipation, we must employ a completely different approach from the one used for an elastic wall (Job et al., 2005).

4.2.2. *The approach of contact force*

In Section 2, we already show that the maximal contact force of a chain impacting on a plate is almost the same as the one of a single sphere. Thus, instead of using the idea of energy partition (Job et al., 2005), we can formulate the maximal contact force on the plate directly using the maximal compression $\max(\overline{\delta}_{\text{p}})$, where $\overline{\delta} = \delta/TV_0$ is the non-dimensional compressive displacement. We have shown in our previous study that $\max(\overline{\delta}_{\text{p}})$ can be approximated by

$$\max(\overline{\delta}_{\text{p}}) = \left(\Pi_4 + \left(\frac{5}{4}\right)^{-\frac{3}{5}}\right)^{-\frac{2}{3}} \tag{28}$$

with an error less than 5% (Peng et al., 2021b). With Eq. (28), we can predict the maximal contact force on the plate by

$$\max(F_{\text{p}}) = \left(\Pi_4 + \left(\frac{5}{4}\right)^{-\frac{3}{5}}\right)^{-1} k_{\text{sp}}^{\frac{2}{5}} m^{\frac{3}{5}} V_0^{\frac{6}{5}} \tag{29}$$

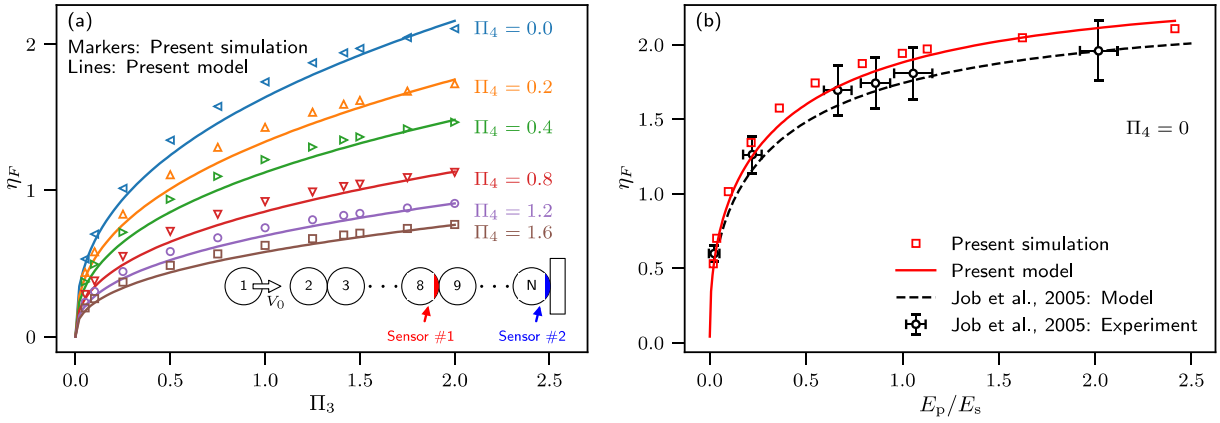

Fig. 11. (a) Comparison between present contact force model with present numerical solutions for systems with $\Pi_4 \in [0, 1.6]$. (b) Model verification of present contact force model with present numerical solution to Eq. (10), Job's model, and Job's experiments (Job et al., 2005) for wall ($\Pi_4 = 0$).

On the other hand, the maximal contact force between the spheres, can be derived based on the fraction of potential energy:

$$\max(F_{\text{chain}}) = k_{\text{ss}}^{\frac{2}{5}}\left(\beta\frac{5}{4}mV_0^2\right)^{\frac{3}{5}} \tag{30}$$

where $\beta \approx 0.44$ is the fraction of potential energy before the HNSW impact on the plate. As a result, we have a model for the contact force ratio (denoted as η_F) considering the compliance of the plate, as follows:

$$\eta_F = \frac{\max(F_{\text{p}})}{\max(F_{\text{chain}})} = \left(\frac{5}{4}\beta\right)^{-\frac{3}{5}}\Pi_3^{\frac{2}{5}}\left(\Pi_4 + \left(\frac{5}{4}\right)^{-\frac{3}{5}}\right)^{-1} \tag{31}$$

To check the proposed model Eq. (31) with the present numerical solutions to Eq. (10) and the results by Job et al. (Job et al., 2005), we computed the contact force ratio η_F by two contact forces: the force between the eighth and the ninth spheres and the one between the end sphere and plate (locations of these force sensors are shown in Fig. 7).

For cases with Π_4 ranging from 0 to 1.6, the present contact force model Eq. (31) agrees with the numerical solution of Eq. (10) as shown in Fig. 11(a). In particular, when Π_4 vanishes for a non-dissipative system (a wall), the present contact force can degrade to Job's model as shown in Fig. 11(b). As a result, the present model fits not only the case with a non-dissipative wall ($\Pi_4 = 0$), but also the cases with plates having a large variation in compliance.

To summarize, in Section 4, by substituting the constant $\alpha = 3.401$ and $\beta = 0.44$, we obtain the two force models as follows:

$$\begin{cases} \eta_A &= e^{-2\Pi_4} \\ \eta_F &= 1.431\Pi_3^{\frac{2}{5}}(\Pi_4 + 0.875)^{-1} \end{cases} \tag{32}$$

5. Identification method for the plate thickness and modulus

5.1. Method description

In Section 4, we have developed two force models: the amplitude ratio of reflected wave η_A and the ratio of the maximal contact force on the plate to the one on the chain η_F. In practice, η_A and η_F can be measured directly by the embedded sensors as shown in Fig. 7. With Eq. (27) and Eq. (31), we can solve for Π_3 and Π_4 simultaneously using the measured force signal η_F and η_A:

$$\begin{cases} \Pi_3 = \eta_F^{\frac{5}{2}}\left(\frac{5}{4}\beta\right)^{\frac{3}{2}}\left(-\frac{5}{3\alpha}\ln\eta_A + \left(\frac{5}{4}\right)^{-\frac{3}{5}}\right)^{\frac{5}{2}} \\ \Pi_4 = -\frac{5}{3\alpha}\ln\eta_A \end{cases} \tag{33}$$

where $\alpha = 3.401$ and $\beta = 0.44$. Using $\Pi_3 = \frac{k_{\text{sp}}}{k_{\text{ss}}}$ and the expression for $\Pi_4 = \lambda$ by Zener (Zener, 1941), we obtain the expression for the Young's modulus and plate thickness:

$$\begin{cases} E_{\text{p}} = \left(\frac{2\sqrt{2}}{\Pi_3} - 1\right)^{-1}\left(\frac{1-\nu_{\text{p}}^2}{1-\nu_{\text{s}}^2}\right)E_{\text{s}} \\ H = \left(\frac{\pi}{2}\right)^{\frac{3}{10}}3^{-\frac{1}{4}}V_0^{\frac{1}{10}}\rho_{\text{p}}^{\frac{1}{20}}\left(\frac{E_{\text{s}}}{1-\nu_{\text{s}}^2}\right)^{-\frac{1}{20}}\left(\frac{\rho_{\text{s}}}{\rho_{\text{p}}}\right)^{\frac{3}{10}}\left(\frac{2\sqrt{2}}{\Pi_3} - 1\right)^{\frac{1}{4}}\Pi_3^{\frac{1}{4}}\Pi_4^{-\frac{1}{2}}R \end{cases} \tag{34}$$

Combining Eq. (33) and Eq. (34), we can identify the plate thickness and Young's modulus simultaneously by measuring the contact forces between the spheres and on the plate as follows:

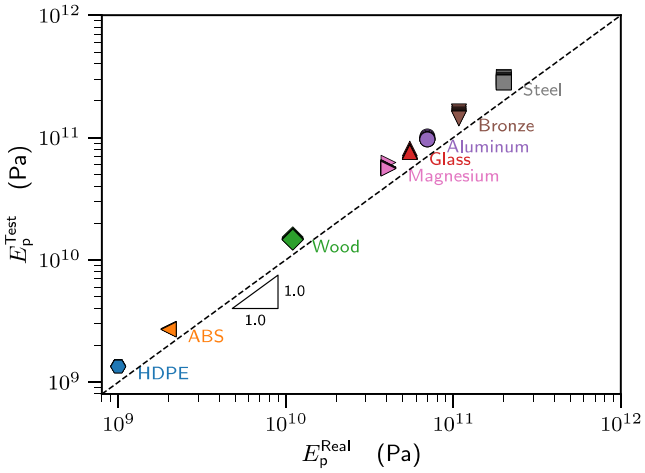

Fig. 12. Identification of Young's modulus using present method. Markers represent all simulated cases (about 70 cases).

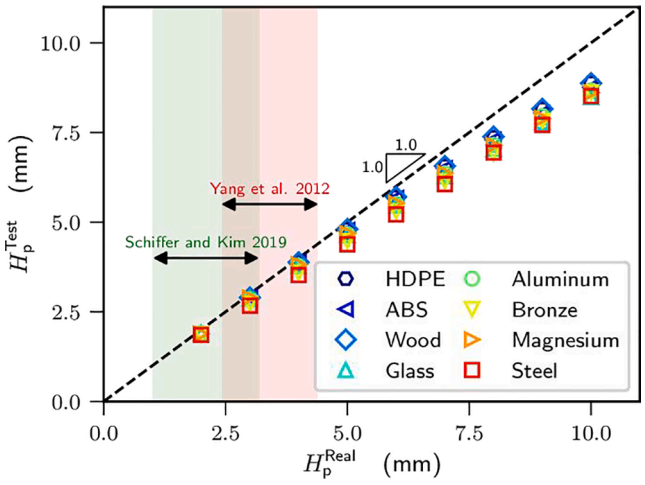

Fig. 13. Identification of Plate thickness using present method. Markers represent all simulated cases (about 70 cases).

$$\begin{cases} E_{\text{p}} = \left(\frac{41.247}{\eta_F^{\frac{5}{2}}(\ln\eta_A^{-1} + 1.785)^{\frac{5}{2}}} - 1\right)^{-1}\left(\frac{1-\nu_{\text{p}}^2}{1-\nu_{\text{s}}^2}\right)E_{\text{s}} \\ H = 0.727V_0^{\frac{1}{10}}\left(\frac{E_{\text{s}}}{1-\nu_{\text{s}}^2}\right)^{-\frac{1}{20}}\rho_{\text{p}}^{-\frac{1}{4}}\rho_{\text{s}}^{\frac{3}{10}}\left(\frac{41.247}{\eta_F^{\frac{5}{2}}(\ln\eta_A^{-1} + 1.785)^{\frac{5}{2}}} - 1\right)^{\frac{1}{4}} \times \\ \qquad \eta_F^{\frac{1}{2}}(\ln\eta_A^{-1} + 1.785)^{\frac{1}{2}}(\ln\eta_A^{-1})^{-\frac{1}{2}}R \end{cases} \tag{35}$$

To verify the present identification method, we conducted finite element method (FEM) analysis using ABAQUS/Explicit, similar to the methods used by previous studies (Nasrollahi and Rizzo, 2020; Schiffer and Kim, 2019).We briefly introduce the simulation parameters here, and the details can be found in Appendix. The granular chain comprised 20 SiC ceramic spheres and a large plate of various combinations of material and thickness. Eight types of common materials were set for the plate separately: high density polyethylene (HDPE), acrylonitrile butadiene styrene plastic (ABS), wood, magnesium, aluminum, bronze, and steel. The thicknesses of plate varied from 2 mm to 10 mm. To model the 20-sphere granular chain, we used 19 point-mass elements and the end sphere meshed with solid elements. The interaction of spheres was presented by nonlinear connectors (compression-only), while the interaction between the end sphere and the plate was established using

the surface contact. The normal behavior was set to 'Hard' contact and the tangent behavior was set to frictional with coefficient 0.1. We also studied the contact without friction, and results show that the friction has a negligible effect. To generate a travelling HNSW, an initial velocity of 0.8 m/s was imposed on the leading point-mass. By requesting output for the force histories of the connectors and the contact of the end sphere and the plate, we computed η_A and η_F, and further calculated the Young's modulus of the plate E_p^{Test} and the plate thickness H_p^{Test} using Eq. (35).

Fig. 12 plots the tested Young's modulus versus the real values for various combinations of material and thickness, exhibiting the feasibility of the proposed method of identification for the Young's modulus of plate. Also, Fig. 13 plots the tested plate thickness versus the real values, where good agreement can also be found. We also plots the thicknesses range used by Yang et al. (Yang et al., 2012) and Schiffer and Kim (Schiffer and Kim, 2019), showing that the present identification is also applicable for the previously studied cases.

5.2. Error analysis

In this section, we check the error transfer relationship from the non-dimensional parameters to the Young's modulus and plate thickness. Differentiating Eq. (34), we obtain:

$$\frac{\Delta E_p}{E_p} = \frac{2\sqrt{2}}{(2\sqrt{2}-\Pi_3)}\frac{\Delta\Pi_3}{\Pi_3} \tag{36}$$

and

$$\frac{\Delta H}{H} = \frac{\left(2\Pi_3+\sqrt{2}\right)}{10\left(2\sqrt{2}-\Pi_3\right)}\frac{\Delta\Pi_3}{\Pi_3} - \frac{1}{2}\frac{\Delta\Pi_4}{\Pi_4} \tag{37}$$

On the one hand, both Eq. (36) and Eq. (37) mean that to minimize the relative error of tested Young's modulus and plate thickness, we can use a chain with high modulus such as ceramics to keep Π_3 small. In the present study, we used a chain of SiC spheres, which have a modulus of 410 GPa, significantly larger than those of most common materials. On the other hand, Eq. (37) also shows that the relative error transfer relationship from Π_4 to the plate thickness is constant.

In summary, for better identification, we recommend using a chain comprising spheres with higher Young's modulus and tune the impact velocity to obtain a clear signal of contact forces.

6. Conclusion and remarks

In this paper, we solved interaction between an HNSW and a large elastic plate by coupling sphere-plate contact with chain dynamics and presented how such interaction is controlled by the two non-dimensional parameters (contact stiffness ratio Π_3 and plate's inelastic parameter Π_4). What is more, we developed an energy dissipation model and two force models which can quantitively connect the effect of interaction on the reflected HNSW to the material and thickness of plate. As a result, we can use these two force models to identify the material and thickness of plate by measuring the amplitude ratio of reflected wave on the chain and the contact force on the plate.

Our work provides a theoretical foundation for the non-destructive evaluation on thin-walled structures using HNSWs. The advantages can be shown in two folds. On the one hand, compared with previous studies on the interaction of an HNSW and a wall (Job et al., 2005; Yang et al., 2011), the present contact force model, Eq.(27) and (31), as well as the present energy dissipation model, Eq. (18), quantitively show that the energy dissipation by flexural wave can be significantly larger than Hunter loss (generally about 5%) and alters the reflection of the HNSW drastically. On the other hand, compared with the studies on the interaction of an HNSW and a dissipative medium (Nasrollahi et al., 2019; Nasrollahi and Rizzo, 2020; Yang et al., 2012), the present model, Eq. (35), provides an explicit and universal formulation of the plate thickness and the mechanical properties from the maximal forces on the chain and on the plate, enabling a wider application of non-destructive evaluation using HNSWs.

In practice, the contact between spheres may introduce some other factors, such as contact plasticity (Peng et al., 2021a; Wang et al., 2017), viscosity (Carretero-González et al., 2009; Liang et al., 2019; Rosas et al., 2007; Vergara, 2010), and adhesion (Thornton et al., 2017). For example, dissipation by viscosity on a chain may alter the profile of the HNSW drastically (Rosas et al., 2007) and hence renders the present method inapplicable. However, these effects can be avoided by using high strength chains with smooth surfaces and moderate impact velocity. In another aspect of practice, we must make sure that the point-force assumption and the large-plate assumption are valid. For the point-force assumption, distinguishable deviation may be expected for the detection of very thin plates if the contact area on plate is comparable to the plate thickness. For such plates, we can choose a granular chain of small spheres and low impact velocity to limit the evaluation error. For the large-plate assumption, we must consider whether the boundary assumption of Zener is valid for a real test. As stated in Section 2.1, if we locate the impact position away from the boundary with a distance of ten times sphere size, we can treat the plate as infinitely large so that the present non-destructive evaluation method can be applied.

Declaration of Competing Interest

The authors declare that they have no known competing financial interests or personal relationships that could have appeared to influence the work reported in this paper.

Acknowledgements

This work was supported by the National Natural Science Foundation of China (12032001, 11890681, 12022210, and 12125202), and the Youth Innovation Promotion Association CAS (2018022).

Appendix:. FEM model

FEM simulations were conducted using ABAQUS commercial software (Dassualt Systèmes, Vélizy-Villacoublay, France) with a dynamic solver (ABAQUS/Explicit). Due to the symmetry, only an axisymmetric model was necessary, shown in Fig. 14. The granular chain comprised nineteen point-masses and one meshed sphere (the 20th sphere). We used connectors to simulate the interaction between neighboring spheres, as well as the interaction between the 19th and 20th spheres. The behavior of the connectors was defined as follows:

$$F_{\text{conn}} = \begin{cases} -k_{\text{ss}}|\delta|^{\frac{3}{2}} & \text{if } \delta < 0 \\ 0 & \text{if } \delta \geq 0 \end{cases}$$

where F_{conn} is the connector force (being negative means compression), and δ is the relative displacement.

The diameter of the end sphere $2R$ was set to 9.53 mm. The radius of the plate was set to 500 mm, sufficiently large to eliminate boundary effects

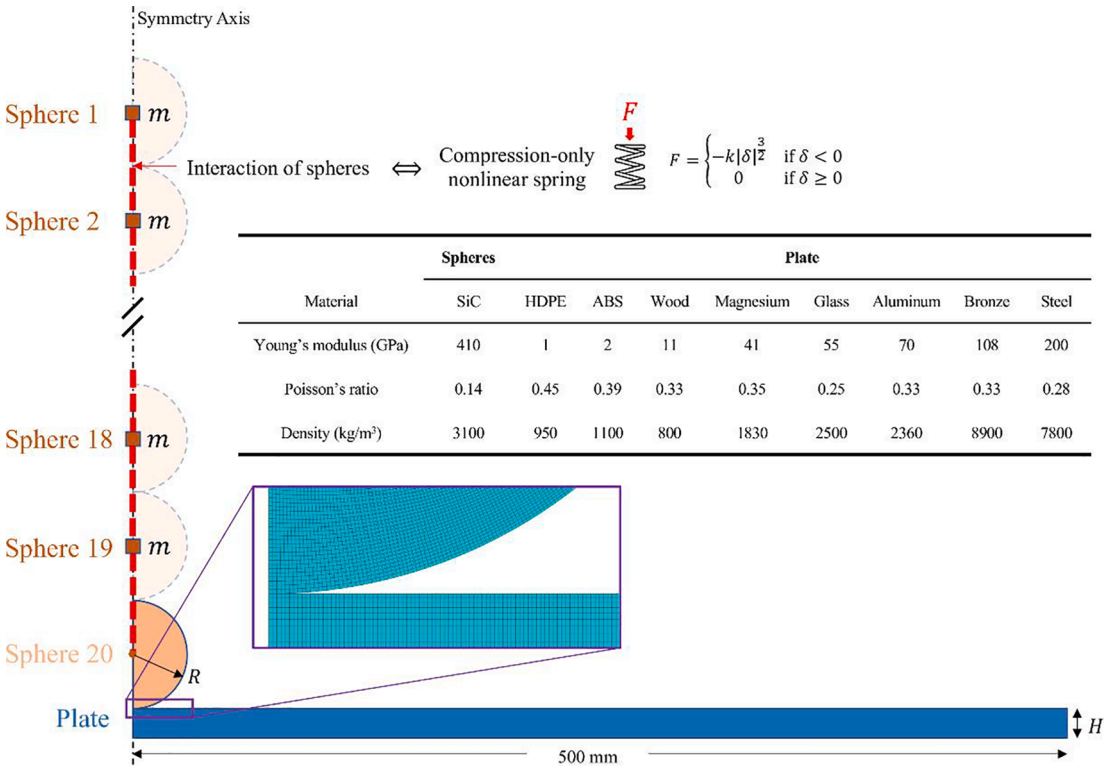

	Spheres				Plate				
Material	SiC	HDPE	ABS	Wood	Magnesium	Glass	Aluminum	Bronze	Steel
Young's modulus (GPa)	410	1	2	11	41	55	70	108	200
Poisson's ratio	0.14	0.45	0.39	0.33	0.35	0.25	0.33	0.33	0.28
Density (kg/m³)	3100	950	1100	800	1830	2500	2360	8900	7800

Fig. 14. FEM model for interaction of solitary wave on granular chain with large plate.

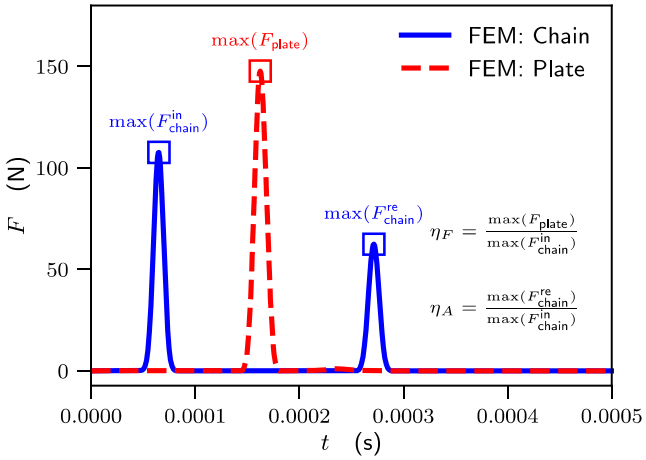

Fig. 15. Typical force histories by FEM simulation: interaction of a chain comprised of 20 SiC spheres with a steel plate with thickness of 3 mm (the diameter of spheres in 9.53 mm and the impact speed is 0.8 m/s).

(possible wave reflection). A contact pair was established between the sphere and the plate: the penalty method of constraint enforcement was applied on the normal direction for the pressure-overclosure relationship ('Hard' contact in ABAQUS), and the friction coefficient was set to 0.1. The material for the elastic sphere was SiC, of which the Young's modulus is 410 GPa, the Poisson's ratio 0.14, and the density 3100 kg/m^3. Also, we set the material of the elastic plate to a variety of common materials: high density polyethylene (HDPE), acrylonitrile butadiene styrene plastic (ABS), wood, magnesium, aluminum, bronze, and steel. Detailed material parameters are listed in the inset of Fig. 14.

The element (CAX4R) count in this model varied from 30,000 to 60,000 depending on the plate thickness, with the finest element size at the contact region being 0.01R. We parametrically studied the cases with various plate thicknesses: $H = 2, 3, \cdots, 10$ mm for each type of material. To generate an HNSW, we set the initial impact velocity for the first point-mass with $V_0 = 0.8$ m/s. To check the force ratios, η_F and η_A, force histories of all the connectors and the contact pair were requested for result output. Using the set material constants as references and calculating the counterparts from force ratios, we could thus validate the proposed identification method for the plate thickness and Young's modulus. Fig. 15 illustrates typical force histories on the chain and on the plate by FEM simulation and how they were used to calculate the force ratios.

References

Berhanu, B., Rizzo, P., Ochs, M., 2012. Highly Nonlinear Solitary Waves for the Assessment of Dental Implant Mobility. J. Appl. Mech. 80.

Cai, L., Rizzo, P., Al-Nazer, L., 2013. On the coupling mechanism between nonlinear solitary waves and slender beams. Int. J. Solids Struct. 50 (25-26), 4173–4183.

Cai, L., Rizzo, P., Li, K., Al-Nazer, L., 2014. Coupling mechanism of granular medium and slender beams, in: Proceedings of SPIE. Presented at the Conference on Nondestructive Characterization for Composite Materials, Aerospace Engineering, Civil Infrastructure, and Homeland Security.

Carretero-González, R., Khatri, D., Porter, M.A., Kevrekidis, P.G., Daraio, C., 2009. Dissipative Solitary Waves in Granular Crystals. Phys. Rev. Lett. 102 (2) https://doi.org/10.1103/PhysRevLett.102.024102.

Chatterjee, A., 1999. Asymptotic solution for solitary waves in a chain of elastic spheres. Phys. Rev. E 59 (5), 5912–5919.

Chaunsali, R., Toles, M., Yang, J., Kim, E., 2017. Extreme control of impulse transmission by cylinder-based nonlinear phononic crystals. J. Mech. Phys. Solids 107, 21–32.

Coste, C., Falcon, E., Fauve, S., 1997. Solitary waves in a chain of beads under Hertz contact. Phys. Rev. E 56 (5), 6104–6117.

Daraio, C., Nesterenko, V.F., Herbold, E.B., Jin, S., 2006. Energy trapping and shock disintegration in a composite granular medium. Phys. Rev. Lett. 96, 4.

Daraio, C., Nesterenko, V.F., Herbold, E.B., Jin, S., 2005. Strongly nonlinear waves in a chain of Teflon beads. Phys. Rev. E 72 (1). https://doi.org/10.1103/PhysRevE.72.016603.

Daraio, C., Ngo, D., Nesterenko, V.F., Fraternali, F., 2010. Highly nonlinear pulse splitting and recombination in a two-dimensional granular network. Phys. Rev. E 82 (3). https://doi.org/10.1103/PhysRevE.82.036603.

Hasan, M.A., Nemat-Nasser, S., 2017. Basic properties of solitary waves in granular crystals. J. Mech. Phys. Solids 101, 1–9.

Hertz, H., 1882. Ueber die Berührung fester elastischer Körper. Journal für die reine und angewandte Mathematik (Crelles Journal) 1882, 156–171.

Herrmann, F., Schmälzle, P., 1981. Simple explanation of a well-known collision experiment. Am. J. Phys. 49 (8), 761–764.

Herrmann, F., Seitz, M., 1982. How does the ball-chain work. Am. J. Phys. 50 (11), 977–981.

Jalali, H., Rizzo, P., 2021. Numerical investigation of the interaction of highly nonlinear solitary waves with corroded steel plates. Int. J. Mech. Sci. 208, 106676. https://doi.org/10.1016/j.ijmecsci.2021.106676.

Jalali, H., Rizzo, P., 2020. Highly nonlinear solitary waves for the detection of localized corrosion. Smart Mater. Struct. 29 (8), 085051. https://doi.org/10.1088/1361-665X/ab9b5b.

Job, S., Melo, F., Sokolow, A., Sen, S., 2005. How Hertzian Solitary Waves Interact with Boundaries in a 1D Granular Medium. Phys. Rev. Lett. 94 (17) https://doi.org/10.1103/PhysRevLett.94.178002.

Khatri, D., Daraio, C., Rizzo, P., 2008. Highly nonlinear waves' sensor technology for highway infrastructures, in: Proceedings of SPIE. Presented at the Conference on Nondestructive Characterization for Composite Materials, Aerospace Engineering, Civil Infrastructure, and Homeland Security 2008.

Kim, E., Yang, J., 2014. Wave propagation in single column woodpile phononic crystals: Formation of tunable band gaps. J. Mech. Phys. Solids 71, 33–45.

Kim, H., Kim, E., Yang, J., 2019. Nonlinear wave propagation in 3D-printed graded lattices of hollow elliptical cylinders. J. Mech. Phys. Solids 125, 774–784.

Lazaridi, A.N., Nesterenko, V.F., 1985. Observation of a new type of solitary waves in a one-dimensional granular medium. J. Appl. Mech. Tech. Phys. 26 (3), 405–408.

Leonard, A., Ponson, L., Daraio, C., 2014. Wave mitigation in ordered networks of granular chains. J. Mech. Phys. Solids 73, 103–117.

Liang, T., Zhu, X.-L., Meng, Z.-C., Duan, W.-S., Yang, L., 2019. Shock Waves in Nonlinear Granular Chain with Viscosity under Hertz Contact. J. Phys. Soc. Jpn. 88 (3), 034002. https://doi.org/10.7566/JPSJ.88.034002.

Liu, Z.-G., Wang, Y.-S., Huang, G., 2019. Solitary waves in a granular chain of elastic spheres: Multiple solitary solutions and their stabilities. Phys. Rev. E 99 (6). https://doi.org/10.1103/PhysRevE.99.062904.

Liu, Z.-G., Zhang, J., Wang, Y.-S., Huang, G., 2021. Analytical solutions of solitary waves and their collision stability in a pre-compressed one-dimensional granular crystal. Nonlinear Dyn. 104 (4), 4293–4309.

MacKay, R.S., 1999. Solitary waves in a chain of beads under Hertz contact. Phys. Lett. A 251 (3), 191–192.

Mueller, P., Boettcher, R., Russell, A., Truee, M., Tomas, J., 2015. A novel approach to evaluate the elastic impact of spheres on thin plates. Chem. Eng. Sci. 138, 689–697.

Nasrollahi, A., Lucht, R., Rizzo, P., 2019. Solitary Waves to Assess the Internal Pressure and the Rubber Degradation of Tennis Balls. Exp. Mech. 59 (1), 65–77.

Nasrollahi, A., Rizzo, P., 2020. Modeling a new dynamic approach to measure intraocular pressure with solitary waves. J. Mech. Behav. Biomed. Mater. 103, 103534. https://doi.org/10.1016/j.jmbbm.2019.103534.

Nesterenko, V.F., 1984. Propagation of nonlinear compression pulses in granular media. J. Appl. Mech. Tech. Phys. 24 (5), 733–743.

Nesterenko, V.F., Daraio, C., Herbold, E.B., Jin, S., 2005. Anomalous wave reflection at the interface of two strongly nonlinear granular media. Phys. Rev. Lett. 95 (15) https://doi.org/10.1103/PhysRevLett.95.158702.

Ngo, D., Fraternali, F., Daraio, C., 2012. Highly nonlinear solitary wave propagation in Y-shaped granular crystals with variable branch angles. Phys. Rev. E 85 (3). https://doi.org/10.1103/PhysRevE.85.036602.

Peng, Q., Jin, Y., Liu, X., Wei, Y.G., 2021a. Effect of plasticity on the coefficient of restitution of an elastoplastic sphere impacting an elastic plate. Int. J. Solids Struct. 222-223, 111036. https://doi.org/10.1016/j.ijsolstr.2021.03.023.

Peng, Q., Liu, X., Wei, Y., 2021b. Elastic Impact of Sphere on Large Plate. J. Mech. Phys. Solids 156, 104604. https://doi.org/10.1016/j.jmps.2021.104604.

Rosas, A., Romero, A.H., Nesterenko, V.F., Lindenberg, K., 2007. Observation of Two-Wave Structure in Strongly Nonlinear Dissipative Granular Chains. Phys. Rev. Lett. 98 (16) https://doi.org/10.1103/PhysRevLett.98.164301.

Schiffer, A., Kim, T.-Y., 2019. Modelling of the interaction between nonlinear solitary waves and composite beams. Int. J. Mech. Sci. 151, 181–191.

Sen, S., Hong, J., Bang, J., Avalos, E., Doney, R., 2008. Solitary waves in the granular chain. Phys. Rep.-Rev. Sect. Phys. Lett. 462 (2), 21–66.

Sen, S., Manciu, M., 2001. Solitary wave dynamics in generalized Hertz chains: An improved solution of the equation of motion. Phys. Rev. E 64, 4.

Sen, S., Manciu, M., Wright, J.D., 1998. Solitonlike pulses in perturbed and driven Hertzian chains and their possible applications in detecting buried impurities. Phys. Rev. E 57 (2), 2386–2397.

Sen, S., Krishna mohan, T.R., Visco, D.P., Swaminathan, S., Sokolow, A., Avalos, E., Nakagawa, M., 2005. Using mechanical energy as a probe for the detection and imaging of shallow buried inclusions in dry granular beds. Int. J. Mod. Phys. B 19 (18), 2951–2973.

Sinkovits, R.S., Sen, S., 1995. Nonlinear Dynamics in Granular Columns. Phys. Rev. Lett. 74 (14), 2686–2689.

Spadoni, A., Daraio, C., 2010. Generation and control of sound bullets with a nonlinear acoustic lens. PNAS 107 (16), 7230–7234.

Thornton, C., Cummins, S.J., Cleary, P.W., 2017. On elastic-plastic normal contact force models, with and without adhesion. Powder Technol. 315, 339–346.

Vergara, L., 2010. Model for Dissipative Highly Nonlinear Waves in Dry Granular Systems. Phys. Rev. Lett. 104 (11) https://doi.org/10.1103/PhysRevLett.104.118001.

Vergara, L., 2005. Scattering of solitary waves from interfaces in granular media. Phys. Rev. Lett. 95 (10) https://doi.org/10.1103/PhysRevLett.95.108002.

Villacreses, J.P., Caicedo, B., Caro, S., Yépez, F., 2021. Feasibility of the use of nonlinear solitary waves for the nondestructive measurement of Young's modulus of rocks and compacted materials. Transp. Geotech. 26, 100437. https://doi.org/10.1016/j.trgeo.2020.100437.

Wang, E., Manjunath, M., Awasthi, A.P., Pal, R.K., Geubelle, P.H., Lambros, J., 2014. High-amplitude elastic solitary wave propagation in 1-D granular chains with preconditioned beads: Experiments and theoretical analysis. J. Mech. Phys. Solids 72, 161–173.

Wang, H., Yin, X., Deng, Q., Yu, B.o., Hao, Q., Dong, X., 2017. Experimental and theoretical analyses of elastic-plastic repeated impacts by considering wave effects. Eur. J. Mech. A. Solids 65, 212–222.

Waymel, R.F., Wang, E., Awasthi, A., Geubelle, P.H., Lambros, J., 2018. Propagation and dissipation of elasto-plastic stress waves in two dimensional ordered granular media. J. Mech. Phys. Solids 120, 117–131.

Yang, F., Xie, W., Meng, S., 2020. Impact and blast performance enhancement in bio-inspired helicoidal structures: A numerical study. J. Mech. Phys. Solids 142, 104025. https://doi.org/10.1016/j.jmps.2020.104025.

Yang, J., Khatri, D., Anzel, P., Daraio, C., 2012. Interaction of highly nonlinear solitary waves with thin plates. Int. J. Solids Struct. 49 (13), 1463–1471.

Yang, J., Restuccia, F., Daraio, C., 2013. Highly Nonlinear Granular Crystal Sensor and Actuator for Delamination Detection in Composite Structures. Structural Health Monitoring 2011: Condition-Based Maintenance and Intelligent Structures.

Yang, J., Silvestro, C., Khatri, D., De Nardo, L., Daraio, C., 2011. Interaction of highly nonlinear solitary waves with linear elastic media. Phys. Rev. E 83 (4). https://doi.org/10.1103/PhysRevE.83.046606.

Yoon, S., Schiffer, A., Kim, J.J., Jang, I.G., Lee, S., Kim, T.-Y., 2020. Numerical predictions of the interaction between highly nonlinear solitary waves and the microstructure of trabecular bone in the femoral head. J. Mech. Behav. Biomed. Mater. 109, 103805. https://doi.org/10.1016/j.jmbbm.2020.103805.

Zener, C., 1941. The Intrinsic Inelasticity of Large Plates. Phys. Rev. 59 (8), 669–673.

Zhang, Q., Potekin, R., Li, W., Vakakis, A.F., 2020. Nonlinear wave scattering at the interface of granular dimer chains and an elastically supported membrane. Int. J. Solids Struct. 182-183, 46–63.